single peak B located between peaks B1 and B2. This indicates the formation of Fe_2TiO_5. The spectra of $TiCl_4$-treated hematite and Fe_2TiO_5 showed a slight difference in the intensity of peak A, attributed to the existence of TiO_2 in the top layer, but the spectra of the HF-Ti-treated (30 s) sample and Fe_2TiO_5 were almost identical because of the ultrathin layer. When the FeOOH sample on an FTO substrate was immersed in Ti-dissolved HF solution, Ti ions adsorbed on the surface of FeOOH; the etching of FeOOH by HF might favor this process. The following annealing in air produced amorphous TiO_2, which reacted with hematite to form an ultrathin layer of Fe_2TiO_5. The Fe_2TiO_5-hematite heterostructure was thus formed to yield satisfactory performance.

In summary, it is revealed by XAS measurment that Fe_2TiO_5 forms a heterojunction with hematite. This heterojunction decreases the photogenerated hole accumulation and improves the performance of hematite. The facile synthesis of the new heterojunction structure became an effective method to improve the performance of hematite for solar oxidation of water. The new Fe_2TiO_5-hematite heterostructure provides insight into understanding the enhanced performance of other Ti-treated hematite nanostructures. (Reported by Yan-Gu Lin)

This report features the work of Xuhui Sun and his co-workers published in ACS Nano ***9****, 5348 (2015).*

Reference

1. J. Deng, X. Lv, J. Liu, H. Zhang, K. Nie, C. Hong, J. Wang, X. Sun, J. Zhong, and S. T. Lee, ACS Nano **9**, 5348 (2015).

Zoom in the Perovskite Solar Cell with X-ray Scattering

Organometal halide-perovskite solar cells attract considerable attention because of their advantages of high performance, low cost, processability in solution, light weight and flexibility. Such perovskite solar cells demonstrate an exciting progress with efficiency of power conversion (PCE) up to 19.3 %. The structure of the perovskite film, generally characterized according to the uniformity, coverage and pin-hole (or gap) between grains, is the critical role strongly affecting the PCE. The crystalline characteristics of the perovskite layer were reported to play important roles affecting the cell performance. These structural properties are closely related to the exciton diffusion, dissociation of charge carriers and transport to the electrodes. The characterization of the structure to correlate with the processing control of a hierarchical structure of a planar heterojunction perovskite layer was, however, incomplete because of the limitations of conventional microscopes (i.e. scanning electron microscope and atomic-force microscope) and X-ray diffraction (XRD). For instance, XRD typically provides limited information because of the existence of preferential orientation of the perovskite grains.

To extend the current structural observations, simultaneous small-angle scattering and wide-angle X-ray scattering at grazing incidence (GISAXS/GIWAXS) techniques are an effective tool to probe quantitatively the hierarchical structure of a phase-separated bulk heterojunction structure in polymer solar cells. In particular, GIWAXS with a two-dimensional (2D) detector can provide sufficient information about crystallinity, including the orientation of all perovskite grains inside the film. Cheng-Si Tsao (Institute of Nuclear Energy Research), U-Ser Jeng (NSRRC) and Chun-Jen Su (NSRRC) cooperatively performed synchrotron-based X-ray-scattering techniques at **BL23A1** to probe quantitatively the hierarchical structure of planar heterojunction perovskite solar cells. The correlation between the crystallization behavior, crystal orientation, internal structure on nano- and meso-scales and surface morphology of the perovskite film as functions of various processing control parameters was discussed.

In Tsao's work, synchrotron GISAXS/GIWAXS measurements were simultaneously performed to characterize quantitatively the multi-length-scale structures of bulk $CH_3NH_3PbI_{3-x}Cl_x$ perovskite films prepared under varied control conditions under (1) sequential vacuum deposition and (2) one-step solution-processed deposition.[1] In the one-step solution-processed deposition method, the evolution of an hierarchical pore-network structure inside the perovskite film into a dense grain structure (no internal pore) with a fractal surface was tuned with preparation parameters. In the sequential vacuum deposition method, a quantitative GISAXS analysis revealed how a fractal surface of densely aggregated grains evolves into a film on tuning the substrate temperature. The corresponding GIWAXS patterns demonstrated the variation of the orientation of crystalline grains and a phase transformation.

For $CH_3NH_3PbI_{3-x}Cl_x$ perovskite films prepared with sequential vacuum deposition, the critical parameter controlling the PCE and film structure is the substrate temperature for the vapor deposition of CH_3NH_3I onto the $PbCl_2$ film. The $CH_3NH_3PbI_{3-x}Cl_x$ perovskite films prepared at substrate temperatures 65, 75 and 85 °C were investigated with the simultaneous synchrotron GISAXS/GIWAXS measurements. Figure 1 shows the GISAXS profiles, $I(Q)$, of the vacuum-deposited $CH_3NH_3PbI_{3-x}Cl_x$ films at substrate temperatures 65, 75 and 85 °C, respectively. The GISAXS profiles show the behavior of a power-law scattering with the characteristic of surface fractal ($I(Q) \propto Q^{-\alpha}$; $3 \le \alpha \le 4$). The exponent α is related to the surface fractal dimension D_s according to $D_s = 6-\alpha$. The surface fractal

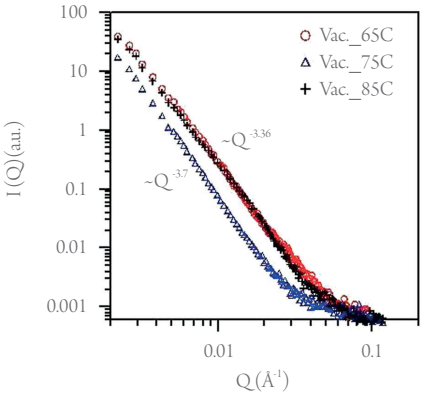

Fig. 1: GISAXS profiles of vacuum-deposited films of $CH_3NH_3PbI_{3-x}Cl_x$ prepared at substrate temperatures 65, 75 and 85 °C, respectively. [Reproduced from Ref. 1]

revealed that the film surface had a morphology of self-similarity at various scales beginning from nanometers. The GISAXS profiles show that the fractal surface morphologies formed at 85 and 65 °C were similar whereas the surface morphology formed at 75 °C showed a larger scale, indicated by the power-law scattering at the smaller Q region. The $CH_3NH_3PbI_{3-x}Cl_x$ film prepared at 75 °C had a much greater PCE (~ 15 %) than those prepared at the other temperatures (6.1 % and 4.5 % for substrate temperatures 65 and 85 °C, respectively). This result is attributed to the film prepared at 75 °C having the greatest crystallinity of $CH_3NH_3PbI_{3-x}Cl_x$. The grain morphology seemed to be closely related to its crystalline structure and quality.

In Fig. 2, all 2D GIWAXS patterns show diffraction rings corresponding to planes (110) and (220) at $Q = 10$ and 20 nm^{-1}, respectively. The crystallites with plane (110) oriented (normal) to the out-of-plane direction dominate for all films. The out-of-plane direction was perpendicular to the substrate or film surface (defined as the Q_z direction marked in the 2D GIWAXS pattern). These oriented crystallites were indicated by the clear diffraction spot in the Q_z direction. The perovskite films prepared at 65 and 75 °C also showed a significant fraction of crystallites having plane (110) oriented to the in-plane direction, as indicated by the diffraction spot in the in-plane direction. This in-plane direction was parallel to the substrate or film surface (defined as the Q_x direction, also marked in Fig. 2). The relative crystallinity was approximately represented by the azimuthally averaged intensity of diffraction ring (110) in the 2D GIWAXS pattern. The perovskite film prepared at 75 °C had the greatest crystallinity and the largest amount of dominant crystallites with plane (110) oriented to the out-of-plane direction, indicated by diffraction spot (110). The new information revealed in this GIWAXS work follows. (I) For the film prepared at 65 °C, a fraction of $CH_3NH_3PbI_{3-x}Cl_x$ crystallites rapidly decomposed into PbI_2 crystallites, as indicated by the appearance of a diffraction spot at $Q = 9$ nm^{-1} in the out-of-plane direction. (II) For the film prepared at 85 °C, a significant decrease of out-of-plane-oriented crystallites was accompanied by the formation of randomly oriented crystallites, indicated by the isotropic distribution of diffraction rings in the 2D GIWAXS pattern (Fig. 2).

This result indicated that the key parameter controlling or tuning the decomposition of vacuum-deposited $CH_3NH_3PbI_{3-x}Cl_x$ crystallites into PbI_2 was the substrate temperature. According to the azimuthally averaged intensities of the GIWAXS patterns, the relative crystallinity of $CH_3NH_3PbI_{3-x}Cl_x$ crystallites prepared at 85 °C exceeded that prepared at 65 °C, but the PCE of the former (4.5 %) was less than that of the latter (6.1 %). The grain boundary (GB) of all randomly oriented crystallites was speculated to form an isotropic distribution of a network. In contrast, the GB network formed by the dominant crystallites with the out-of-plane orientation (normal to the film surface) had an alignment structure that was more favorable to transport charge carriers. In general, GB plays a beneficial role in collecting charge carriers efficiently. The influence of crystal orientation on the PCE was revealed to be larger than that of crystallinity, showing the importance of the crystallites with the out-of-plane orientation. This case became critical for the films without a high crystallinity. The high temperature of the substrate was the factor controlling changing the crystal orientation from a dominant out-of-plane orientation to a random or isotropic orientation.

Figure 3 shows GISAXS profiles of the one-step solution-processed $CH_3NH_3PbI_{3-x}Cl_x$ films prepared with chloride at 0, 10, 20 and 40 %, respectively. The GISAXS profiles prepared with

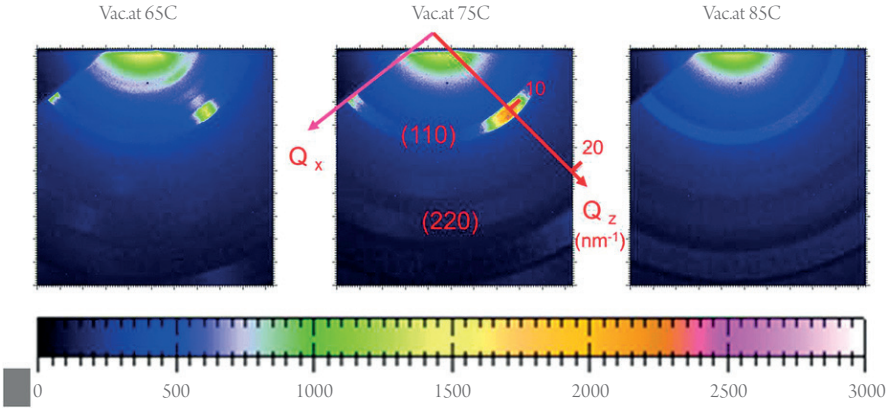

Fig. 2: 2D GIWAXS patterns corresponding to vacuum-deposited $CH_3NH_3PbI_{3-x}Cl_x$ films prepared at substrate temperatures 65, 75 and 85 °C, respectively. [Reproduced from Ref. 1]

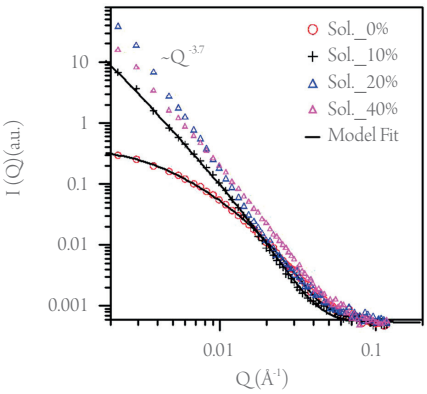

Fig. 3: GISAXS profiles of one-step solution-processed $CH_3NH_3PbI_{3-x}Cl_x$ films prepared with chloride at 0, 10, 20 and 40 %, respectively. [Reproduced from Ref. 1]

chloride at 0 and 10 % showed the behavior of a power-law scattering ($I(Q) \propto Q^{-\alpha}$; $1 \le \alpha \le 3$) in the middle Q range (0.007 ~ 0.03 $Å^{-1}$). Here, the exponent values, α, reveal the typical characteristics of mass fractals. The only best-fit model must include a structure factor of a fractal network consisting of the primary particles or pores. The GISAXS pattern is contributed mainly by the morphology of the multi-length-scale fractal network structure formed from the aggregation of primary pores here. Interestingly, the GISAXS profile (Fig. 3) of the perovskite film prepared with chloride (10 %) demonstrates a distinctive fractal pore network. The radius of the primary pores, pore fractal dimension and network domain determined with a model analysis were significantly enhanced to 4.0 nm, 2.6 and 115 nm, respectively. Notably, when the chloride fraction was increased to 20 %, a nearly fully covered film was formed. The corresponding GISAXS profile (Fig. 3) shows a power-law scattering with the characteristic of surface fractal morphology ($I(Q) \propto Q^{-\alpha}$; $\alpha = 3.7$; $D_s = 2.3$) having a dense internal structure. It was explained that the compact and highly dense aggregation of perovskite grains forced the internal pores to collapse into a dense structure with fractal morphology only on the surface. Moreover, when the chloride fraction increased to 40 %, the aggregation of grains into a film became over-coalescent; there thus appeared a few holes between large grains. The corresponding GISAXS profile shows a surface fractal morphology with fractal dimension α ~ 3.0 ($D_s = 3$). The increased surface fractal dimension reflected that the surface became rougher.

The GIWAXS result (Fig. 4) was also reasonably correlated with PCE values. According to the 2D GIWAXS patterns, a comparison between the intensities of the out-of-plane (110) diffraction spots of perovskite crystallites (in the Q_z direction in Fig. 4) demonstrated a substantial difference in

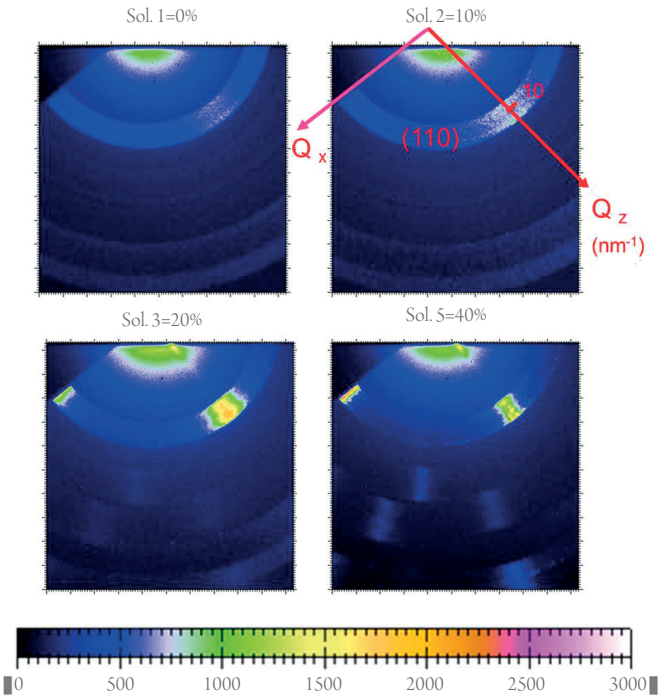

Fig. 4: 2D GIWAXS patterns of one-step solution-processed $CH_3NH_3PbI_{3-x}Cl_x$ films prepared with chloride 0, 10, 20 and 40 %, respectively. [Reproduced from Ref. 1]

order 20 % > 40 % > 10 % > 0, consistent with the performance. This result revealed that the simultaneous GISAXS/GIWAXS analysis enabled a complete interpretation of the relation between structure and performance. The crystallites with a strong out-of-plane orientation (i.e. the direction normal to the film surface) of plane (110), shown by 2D GIWAXS (or GIXRD) measurement, was closely related to the high device performance. The GB network formed by the dominant crystallites with an out-of-plane orientation (normal to the film surface) was speculated to have an alignment structure that was more favorable to the transport of charge carriers than that of crystallites with other orientations. For perovskite films with an internal pore network (prepared with chloride 0 and 10 %), the crystallites oriented to the out-of-plane direction dominated; no crystallite with the in-plane orientation was apparently observed. The dense perovskite films with surface fractal morphology (prepared with chloride 20 % and 40 %) had crystallites with both out-of-plane and in-plane orientations. The film with over-coalesced grains (chloride 40 %) had a highly ordered perovskite structure (shown by other spots at the high Q region between Q_z and Q_x directions in Fig. 4).

In summary, the structural characterization correlated with the processing control of hierarchical structure of a planar heterojunction perovskite layer was incomplete due to the limitations of conventional microscopes and XRD. The GISAXS/ GIWAXS measurement here provided a comprehensive understanding of the concurrent evolution of the film morphology and crystallization correlating with high performance. This result could provide insight into the mechanism of formation and a rational synthesis design. (Reported by Yan-Gu Lin)

This report features the work of Cheng-Si Tsao and his co-workers published in Sci. Rep. ***5****, 13657 (2015).*

References

1. Y. C. Huang, C. S. Tsao, Y. J. Cho, K. C. Chen, K. M. Chiang, S. Y. Hsiao, C. W. Chen, C. J. Su, U. S. Jeng, and H. W. Lin, Sci. Rep. **5**, 13657 (2015).
2. H. C. Liao, C. S. Tsao, M. H. Jao, J. J. Shyue, C. P. Hsu, Y. C. Huang, K. Y. Tian, C. Y. Chen, C. J. Su, and W. F. Su, J. Mater. Chem. A **3**, 10526 (2015).